The efficient production of **1** by *S. erythraea* mutants TED8 and TER43 proves that the multienzyme components of modular PKSs are capable of functioning independently (*14*). In addition, production of **1** by these strains demonstrates that the attachment of an additional COOH-terminal domain has not perturbed the other enzyme activities in the DEBS1 multienzyme. We also wished to determine whether an active thioesterase domain was required for efficient chain termination and cyclization or whether the mere presence of an additional COOH-terminal domain would suffice to disrupt the normal chain transfer between DEBS1 and DEBS2 and hence promote adventitious cyclization. This was done by mutagenesis of the DNA from *eryAIII* encoding the cyclase domain, so that the active site serine residue, Ser3029 (DEBS3 numbering) (*3*, *12*), was altered to an alanine (Fig. 2) (*16*). The mutant domain was used to replace the wild-type cyclase domain in *S. erythraea* strain TER43, by recombination (Fig. 2), to create strain TEDS3029A. This strain produced, under comparable conditions of fermentation, less than 1% of the amount of triketide lactone accumulated by strain TED8, as judged by mass spectrometry (Fig. 3), providing evidence that the cyclase directly accelerates chain termination. On a molar basis, the amount of lactone (10 to 15 mg/liter) produced by the DEBS1 fused to active cyclase was only slightly less than the amount of erythromycin produced by the wild-type strain. In contrast, the unmodified DEBS1, even when very highly expressed in *S. coelicolor*, has been reported to produce only 1 to 3 mg/liter of the lactone, by unknown mechanisms (*12*). Cyclase-promoted cleavage is therefore the method of choice to redirect polyketide synthesis to the formation of chains of specified length.

We have previously shown that the NH_2-terminal acyltransferase-acyl carrier protein di-domain of DEBS1 also behaves as an autonomous functional unit after limited proteolysis under native conditions (*17*), but it remains to be determined whether this domain may also be relocated so as to initiate polyketide chain synthesis at a desired point within a modular PKS. Meanwhile, the recombinant DEBS1-cyclase functional unit is much smaller and more amenable to structure-function analysis than the entire PKS, and its study, either in *S. erythraea* or in heterologous systems (*11*, *18*), should provide further detailed insights into the chemistry and stereochemistry of polyketide chain growth.

REFERENCES AND NOTES

1. D. A. Hopwood and D. H. Sherman, *Annu. Rev. Genet.* **24**, 37 (1990); J. Staunton, *Angew. Chem. Int. Ed. Engl.* **30**, 1302 (1991).
2. J. Beck, S. Ripka, A. Siegner, E. Schultz, E. Schweizer, *Eur. J. Biochem.* **192**, 487 (1990); M. J. Bibb, S. Biro, H. Motamedi, J. F. Collins, C. R. Hutchinson, *EMBO J.* **8**, 2727 (1989); D. H. Sherman *et al.*, *ibid.*, p. 2717; M. A. Fernandez-Moreno, E. Martinez, L. Bots, D. A. Hopwood, F. Malpartida, *J. Biol. Chem.* **267**, 19278 (1992); J. S. Ye *et al.*, *J. Bacteriol.* **176**, 6270 (1994).
3. J. Cortes, S. F. Haydock, G. A. Roberts, D. J. Bevitt, P. F. Leadlay, *Nature* **348**, 176 (1990).
4. S. Donadio, M. J. Staver, J. B. McAlpine, S. J. Swanson, L. Katz, *Science* **252**, 675 (1991); *Gene* **115**, 97 (1992).
5. D. J. MacNeil *et al.*, *Gene* **115**, 97 (1992).
6. A. F. A. Marsden *et al.*, *Science* **263**, 378 (1994).
7. P. Caffrey, D. J. Bevitt, J. Staunton, P. F. Leadlay, *FEBS Lett.* **304**, 225 (1992).
8. S. Donadio, J. B. McAlpine, P. J. Sheldon, M. Jackson, L. Katz, *Proc. Natl. Acad. Sci. U.S.A.* **90**, 7119 (1993).
9. P. F. Leadlay *et al.*, *Biochem. Soc. Trans.* **21**, 218 (1993).
10. A. K. Joshi and S. Smith, *J. Biol. Chem.* **268**, 22508 (1993).
11. C. M. Kao, L. Katz, C. Khosla, *Science* **265**, 509 (1994).
12. C. M. Kao, G. L. Luo, L. Katz, D. E. Cane, C. Khosla, *J. Am. Chem. Soc.* **116**, 11612 (1994).
13. P. Caffrey *et al.*, *Eur. J. Biochem.* **195**, 823 (1991).
14. DEBS2 and DEBS3 were absent from strains TED8 and TER43, as judged by immunoblots of proteins in cell-free extracts.
15. Trace amounts of **1** have been previously isolated from the mother liquor of an *S. erythraea* mutant specifically deleted in DEBS3 (*4*).
16. A strain of *S. erythraea* bearing this single mutation in *eryAIII* is unable to synthesize any macrolides (G. A. Roberts, unpublished data).
17. J. A. Aparicio, P. Caffrey, A. F. A. Marsden, J. Staunton, P. F. Leadlay, *J. Biol. Chem.* **269**, 8524 (1994).
18. G. A. Roberts, J. Staunton, P. F. Leadlay, *Eur. J. Biochem.* **214**, 305 (1993).
19. J. M. Weber *et al.*, *J. Bacteriol.* **172**, 2372 (1990).
20. T. Kaneda, J. C. Butte, X. Taubman, J. W. Corcoran, *J. Biol. Chem.* **237**, 322 (1962).
21. The TCC codon for serine-3029 in the active site of the cyclase was substituted by GCC (alanine). A second mutation was also introduced to convert the GGT codon for glycine at position 3027 to a GCC codon, a silent mutation that introduces an Nae I site as a marker for mutant identification. Two partly complementary oligonucleotides 5′-GGAGTGGCCGGCCACCACGAACGG-3′ and 5′-TGGTGGCCGGCCACGCCGCGGGGGCACT-3′ were used to create the mutations. Each was used in a separate polymerase chain reaction (PCR) with, as template, a 627–base pair Sma I fragment of *eryAIII* in pUC18 that contains codon 3029, and with the appropriate pUC sequencing primer as the second primer. The two PCR products were each cut with Sma I, cloned into pUC18, cut with Nae I, and ligated together. The Sma I insert from a 2.2-kbp Sac I DNA fragment containing the 3′ end of *eryAIII* and cloned into pUC18 was then exchanged with the mutant Sma I fragment, to provide a larger target for recombination (Fig. 2).
22. A. Cutter and J. Staunton, unpublished data.

23. Supported by grants from the Biotechnology and Biological Sciences Research Council and the Engineering and Physical Sciences Research Council.

18 January 1995; accepted 21 March 1995

Crystal Structure of a Purple Acid Phosphatase Containing a Dinuclear Fe(III)-Zn(II) Active Site

Norbert Sträter,*† Thomas Klabunde,† Paul Tucker, Herbert Witzel, Bernt Krebs‡

Kidney bean purple acid phosphatase (KBPAP) is an Fe(III)-Zn(II) metalloenzyme resembling the mammalian Fe(III)-Fe(II) purple acid phosphatases. The structure of the homodimeric 111-kilodalton KBPAP was determined at a resolution of 2.9 angstroms. The enzyme contains two domains in each subunit. The active site is located in the carboxyl-terminal domain at the carboxy end of two sandwiched βαβαβ motifs. The two metal ions are 3.1 angstroms apart and bridged monodentately by Asp^{164}. The iron is further coordinated by Tyr^{167}, His^{325}, and Asp^{135}, and the zinc by His^{286}, His^{323}, and Asn^{201}. The active-site structure is consistent with previous proposals regarding the mechanism of phosphate ester hydrolysis involving nucleophilic attack on the phosphate group by an Fe(III)-coordinated hydroxide ion.

Purple acid phosphatases (PAPs) catalyze the hydrolysis of activated phosphoric acid esters and anhydrides like adenosine triphosphate at a pH range from 4 to 7 (*1*). The characteristic purple color results from a tyrosine→Fe(III) charge transfer transition at ~560 nm. The intensively studied monomeric mammalian enzymes contain an antiferromagnetically coupled Fe(III)-Fe(II) center, whereas KBPAP is dimeric with an Fe(III)-Zn(II) center in both subunits. The physiological function of these enzymes has yet to be established. In addition to a hydrolytic function, a role in the activation of dioxygen by the two-metal center has been discussed at least for the mammalian PAPs (*2*, *3*). PAPs have also attracted considerable interest with respect to their active site structure in comparison to other diiron proteins that use a two-metal-ion mechanism in the activation and transport of dioxygen.

N. Sträter, T. Klabunde, B. Krebs, Anorganisch-Chemisches Institut, Universität Münster, 48149 Münster, Germany.
P. Tucker, European Molecular Biology Laboratory, 69117 Heidelberg, Germany.
H. Witzel, Institut für Biochemie, Universität Münster, 48149 Münster, Germany.

*Present address: Gibbs Chemical Laboratory, Harvard University, Cambridge, MA 02138, USA.
†These authors contributed equally to this work.
‡To whom correspondence should be addressed.

KBPAP contains 432 amino acid residues and five heterogeneous glycosylation sites per monomer (*4*, *5*). The enzyme could be crystallized (*6*) and the three-dimensional structure has been solved by multiple isomorphous replacement with tungstate, a strong inhibitor, bound to the dinuclear metal center as one heavy-atom derivative. A model containing residues 9 to 432, the two metal ions, and five *N*-acetylglucosamine residues was built from phase-improved multiple isomorphous replacement electron density maps and subsequently refined at 2.9 Å resolution in space group $C222_1$. The present model has a crystallographic R factor of 19.6% and shows good stereochemistry (Table 1).

The homodimeric enzyme with a cystine bridge connecting both subunits (*4*) was found to have the shape of a twisted heart with overall dimensions 40 by 60 by 75 Å (Fig. 1). The two dinuclear metal centers are 35 Å apart and are at the bottom of a broad pocket formed by both monomers. Access to the active site is not under the control of any channels or deep canyons in the native protein conformation. The disulfide bridge (Cys^{345}) is located between the two long loops in the upper part of the dimer in Fig. 1. Additional interactions between the monomers occur primarily between the helices α5 and between the loops from residues 253 to 260.

Each monomer consists of two domains. The smaller NH_2-terminal domain is located in the lower part of the dimer in Fig. 1 and does not participate in any interactions between the two monomers or with the active site. It is ~120 amino acid residues long and is composed of two sandwiched β sheets, each containing three antiparallel β strands. A long, curved β strand (β4) shields one edge of the sandwich. The function of the NH_2-terminal domain remains unclear. The COOH-terminal domain containing the active site comprises amino acid residues 120 to 432 and can be classified as an α/β-type structure. It has two rather large mixed β sheets consisting of 6 (β8 to β10, β20 to β22) and 7 (β11 to β15, β18, β19) β strands. The two β sheets are sandwiched on top of one another. The smaller sheet has three parallel strands (β8 to β10), whereas in the larger sheet four strands are parallel (β12 to β14, β18). Alpha Helices (α1, α2, α4, and α5) connect the parallel strands. The two sandwiched motifs, each comprising three parallel β strands and two helices, are connected by helix α3 and β strand β11.

All ligands of the dinuclear metal site are contributed by the amino acid residues of the loops at the carboxy ends of β strands β8 to β10 and β13 to β14. The iron is coordinated by Tyr^{167}, which is obviously responsible for the charge transfer band at 560 nm and the purple color, by the N_ε of His^{325}, and monodentately by the carboxylate group of Asp^{135} (Figs. 2 and 3). The zinc is ligated by the N_ε of His^{286}, the N_δ of His^{323}, and the amide oxygen of Asn^{201}. The two metal ions in the active site are bridged by the monodentate carboxylate group of Asp^{164}. We carefully considered the more commonly observed bridging bidentate mode, but the electron density, the main and side chain geometry, and the behavior of the residue during refinement strongly favor the bridging mode via one oxygen. The refined metal-ligand distances are shown in Table 2. The metal-metal distance has been refined to 3.1 Å.

As might be expected at a resolution of 2.9 Å, the electron density map reveals no unambiguous indication of water, hydroxide, or oxide ligands in the vicinity of the two-metal site. However, on the basis of the observed coordination geometry of the metal ions, on the reaction path, and on spectroscopic studies (*2*, *7*, *8*), we modeled three exogenous ligands into the coordination sphere of the dinuclear center shown in Fig. 3: a terminal hydroxo ligand coordinated to iron (Fe-O 1.9 Å), a terminal aqua ligand coordinated to zinc (Zn-O 2.2 Å), and a μ-hydroxo bridge (Fe-O 1.9 Å, Zn-O 2.1 Å). The two terminal solvent ligands are about 2.8 Å apart in this model and therefore within hydrogen bonding distance. Whereas the zinc coordination sphere matches a distorted octahedron, the symmetry of the iron ligand sphere is almost perfectly octahedral with respect to the angles around the metal (Fig. 3). Alternative models for the exogenous solvent ligands (two bridging, no terminal; one bridging, one terminal; or one bridging, no terminal) have also been considered. However, the geometry of the coordination sphere around the metal ions strongly favors the model presented in Fig. 3.

According to the postulated reaction path (*2*, *7*, *8*) of the PAPs we assume that the phosphate group of the substrate interacts with the zinc, thereby displacing the water ligand. This is in agreement with the results of Aquino *et al.* (*8*). By a S_N2-type attack of the iron-bound hydroxo ligand, the alcohol component would be released with inversion of the absolute configuration at

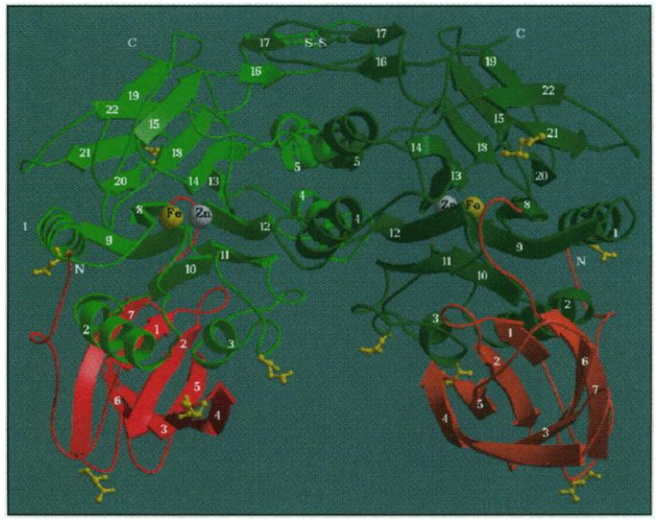

Fig. 1. Ribbon diagram (*20*) of the KBPAP dimer. The two metal ions are shown as spheres (Fe yellow, Zn gray) and the cystine bridge and the glycosylated asparagine side chains are drawn as ball and stick models.

Table 1. Diffraction data, phasing, density averaging, and refinement statistics for KBPAP (*22*). Abbreviations are defined as follows: d_{min} is the minimum Bragg spacing or λ\2 sin θ, where λ is the x-ray wavelength and θ is half the diffraction angle; $R_{merge}=\Sigma_{hkl}\Sigma_i|I_i - \langle I\rangle|/\Sigma\langle I\rangle$, where I_i is the intensity measurement of a particular symmetry-related reflection; $R_{iso}=\Sigma(||F_{PH}| - |F_P||)/\Sigma|F_P|$, where F_P and F_{PH} are the structure factor amplitudes of the native protein and protein complexed with heavy atoms, respectively. Phasing power = $\Sigma(|F_H(calc)|/\Sigma|E|)$, where F_H is the structure factor of the heavy atoms and E (lack of closure error) = $|F_{PH}(obs)| - |F_{PH}(calc)|$. PIP is di-μ-iodobis(ethylenediamine)-diplatinum (II) nitrate.

Data	d_{min} (Å)	Unique reflections (no.)	Completeness (%)	R_{merge} (%)	R_{iso} (%)	Sites (no.)	Phasing power
Native	2.9	62,025	93.7	9.8			
Na_2WO_4 (1 mM)	3.5	34,686	91.4	10.8	14.7	4	1.1
PIP (2.5 mM)	3.5	24,127	63.6	12.5	18.6	8	1.0
PIP (1.5 mM)	3.5	20,157	53.1	11.4	14.6	4	0.6

the phosphorus atom (9). The histidines 202 and 296 as well as Arg^{258} of the other subunit may interact with the phosphate group of the substrate (Fig. 2B) in such a way as to stabilize a pentacoordinate phosphorus transition state. Other side chains that could participate in interactions with the substrate include Tyr^{365}, His^{295}, and Glu^{299}. A small, polar cavity about 9 Å apart from the zinc ion is found in the region of Tyr^{256}, His^{253}, Ser^{287}, Ser^{252}, and Lys^{306} from the other monomer. $|F_o| - |F_c|$ electron density maps revealed that this cavity is occupied by a nonprotein ligand, which may be sulfate from the isolation procedure or acetate from the crystallization buffer. It remains to be shown whether this cavity is part of a binding site for the still unknown natural substrates, which may also include larger molecules like phosphoproteins.

The active site of KBPAP seems to be similar to that of the mammalian Fe(III)-Fe(II) PAPs. After exchange of Zn(II) for Fe(II), KBPAP shows nearly identical spectroscopic and kinetic behavior to the mammalian enzymes (*2*, *10*). Evidence for one tyrosine and one N_ε-coordinated histidine to iron(III) and the ligation of one N_δ-coordinated histidine to iron(II) could be obtained by paramagnetically shifted proton resonances in nuclear magnetic resonance studies (*11*). The presence of a carboxylate group has been concluded from nuclear Overhauser and exchange spectroscopy experiments (*12*). Additional ligands could not be unambiguously identified. Thus, evidence for similarity of the active site in plant and mammalian PAPs is provided, despite the lack of any sequence homology. In contrast, some differences should also be considered. We cannot explain why the absorption maximum of the Fe(III)-Fe(III) KBPAP does not shift from 560 to 515 nm after reduction as observed for the mammalian enzymes (*2*). EXAFS studies on the mammalian PAPs reveal metal-metal distances of 3.00 Å for the bovine spleen enzyme (*13*) and 3.15 Å or 3.52 Å for uteroferrin (*14*). The 3.9 Å metal-metal distance determined for KBPAP by EXAFS measurements on frozen solutions (*15*) is not consistent with our x-ray data and even exceeds the error limit of the crystal structure determination. Further EXAFS measurements are under way to reexamine the value determined with previous data.

The structure and location of the active site of KBPAP differs considerably from the diiron proteins hemerythrin (*16*), ribonucleotide reductase (*17*), and methane monooxygenase (*18*), which are all involved in transport or activation of dioxygen. In contrast to these proteins, the coordination sphere of the dinuclear metal site in KBPAP comprises, in addition to histidines and carboxylate groups, one tyrosine and one asparagine. Furthermore, the active site of KBPAP is located at the carboxy end of two sandwiched β sheets, whereas in the other diiron proteins the metal core is buried between the α helices of a four-helix bundle.

Alkaline phosphatase, a trinuclear Zn-Zn-Mg metalloenzyme with a Zn-Zn dis-

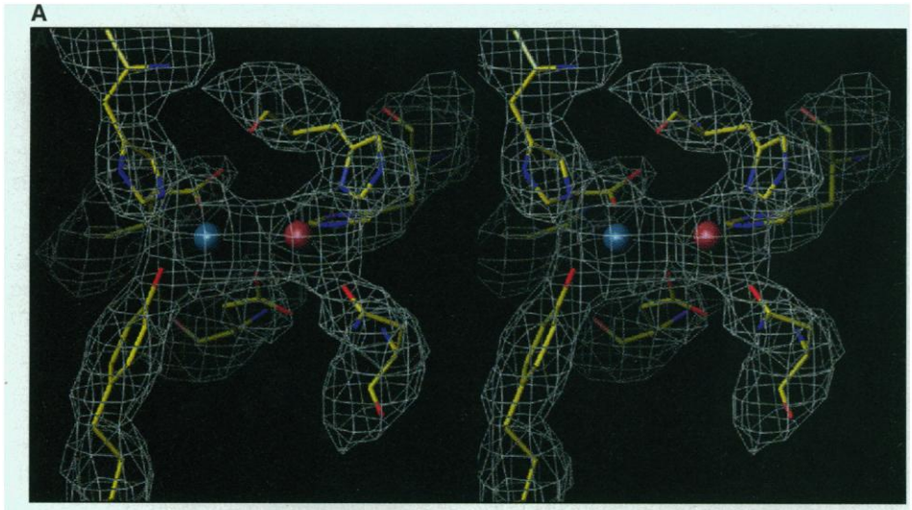

Fig. 2. Active site region of KBPAP. (**A**) $2|F_o| - |F_c|$ electron density map contoured at two times the rms deviation of the map (stereo view). The zinc is shown in red and the iron in blue. Carbons are colored yellow, oxygens red, and nitrogens blue. The final $|F_o| - |F_c|$ maps show that acetate, which was present in the crystallization buffer, has not bound to the metal cluster. (**B**) Residues that might participate in substrate binding. The backbone of the other subunit of the dimer is colored in gold. The small, polar cavity shown in green was calculated by the program Voidoo (*21*).

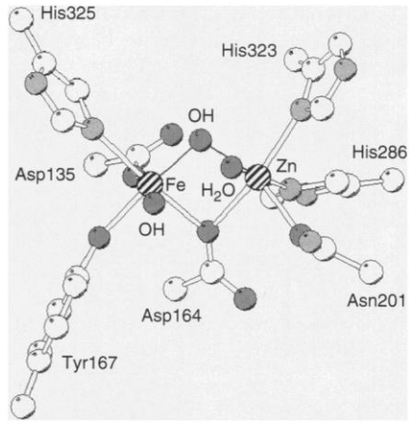

Fig. 3. Model of the dinuclear metal center and the ligands. The three exogenous solvent ligands shown in thin lines have been placed solely on the basis of the observed coordination geometry around the metal ions. The solvent ligands could not be unambiguously identified by the 2.9 Å electron density and are not part of the crystallographic model. Their presence is based on the proposed reaction path and on spectroscopic studies. The figure was prepared with Molscript (*20*).

Table 2. Refined metal-ligand distances (in angstroms) for the four subunits (A to D) in the asymmetric unit.

Metal ion	Ligand atom	A	B	C	D
Zn(II)	Asp^{164}, $O_{\delta 1}$	2.2	2.2	2.3	2.2
	Asn^{201}, $O_{\delta}1$	2.2	2.3	2.3	2.2
	His^{286}, N_ε	2.1	2.1	2.1	2.1
	His^{323}, N_δ	2.3	2.3	2.2	2.3
Fe(III)	Asp^{135}, $O_{\delta 1}$	2.0	2.0	2.0	2.0
	Asp^{164}, $O_{\delta 1}$	2.2	2.2	2.2	2.1
	Tyr^{167}, O	2.2	2.1	2.2	2.1
	His^{325}, N_ε	2.4	2.4	2.4	2.5

tance of 3.9 Å, resembles KBPAP in its two-metal–ion mechanism (*19*). Although the phosphate ester hydrolysis of alkaline phosphatase proceeds via a phosphoseryl intermediate with retention of the overall configuration at the phosphorus, the functional role of both metals is similar compared to that of the metals in the PAPs: One zinc ion primarily binds and preorients the phosphate group of the phosphoseryl intermediate for the attack of the water ligand that was activated by the other zinc ion. The weaker Lewis-acidity of zinc(II) compared to iron(III) leads to the shift of the phosphatase reaction to the alkaline side.

The first structure of a purple acid phosphatase presented here forms the structural basis for understanding the hydrolytic action of this enzyme class on phosphate esters. The results are consistent with the models for the dimetal center and with the proposed mechanism on the basis of several spectroscopic and kinetic studies, albeit the detailed structural and functional relation between the mammalian enzymes and the kidney bean PAP remains to be established.

REFERENCES AND NOTES

1. K. Doi, B. L. Antanaitis, P. Aisen, *Struct. Bonding* **70**, 1 (1988); L. Que Jr. and A. E. True, *Prog. Inorg. Chem.* **38**, 97 (1990); J. B. Vincent, G. L. Olivier-Lilley, B. A. Averill, *Chem. Rev.* **90**, 1447 (1991).
2. H. Suerbaum *et al.*, *Eur. J. Biochem.* **214**, 313 (1993).
3. A. R. Hayman and T. M. Cox, *J. Biol. Chem.* **269**, 1294 (1994).
4. T. Klabunde *et al.*, *Eur. J. Biochem.* **226**, 369 (1994).
5. B. Stahl *et al.*, *ibid.* **220**, 321 (1994).
6. N. Sträter *et al.*, *J. Mol. Biol.* **224**, 511 (1992).
7. M. Dietrich, D. Münstermann, H. Suerbaum, H. Witzel, *Eur. J. Biochem.* **199**, 105 (1991).
8. M. A. S. Aquino, J.-S. Lim, A. G. Sykes, *Chem. Soc. Dalton Trans.* 429 (1994).
9. E. G. Mueller, M. W. Crowder, B. A. Averill, J. R. Knowles, *J. Am. Chem. Soc.* **115**, 2974 (1993).
10. J. L. Beck *et al.*, *Biochim. Biophys. Acta* **869**, 61 (1986).
11. Z. Wang *et al.*, *Biochemistry* **31**, 5263 (1992).
12. R. C. Holz, L. Que Jr., L.-J. Ming, *J. Am. Chem. Soc.* **114**, 4434 (1992).
13. S. M. Kauzlarich, B. K. Teo, S. Burman, J. C. Davis, B. A. Averill, *Inorg. Chem.* **25**, 2781 (1986).
14. A. E. True, R. C. Scarrow, C. R. Randall, R. C. Holz, L. Que Jr., *J. Am. Chem. Soc.* **115**, 4246 (1993).
15. S. Priggemeyer *et al.*, *Inorg. Chem.* **34**, 1445 (1995).
16. M. A. Holmes, I. L. Trong, L. Turley, L. C. Sieker, R. E. Stenkamp, *J. Mol. Biol.* **218**, 583 (1991).
17. P. Nordlund, B.-M. Sjöberg, H. Eklund, *Nature* **345**, 593 (1990).
18. A. C. Rosenzweig, C. A. Frederick, S. J. Lippard, P. Nordlund, *ibid.* **366**, 537 (1993).
19. E. E. Kim and H. W. Wyckoff, *J. Mol. Biol.* **218**, 449 (1991).
20. P. J. Kraulis, *J. Appl. Crystallogr.* **24**, 946 (1991).
21. G. J. Kleywegt and T. A. Jones, *Acta Crystallogr. Sect. D*, in press.
22. Two crystal forms were used for the structure determination: tetragonal crystals of space group $P4_32_12$ with unit cell dimensions a = b = 104.4 and c = 309.9 Å (*6*) and orthorhombic crystals of space group $C222_1$ with a = 132.7, b = 347.3, and c = 128.7 Å. The asymmetric unit contains two and four subunits for the $P4_32_12$ and the $C222_1$ space group, respectively. Because of the higher diffraction limit of 2.9 Å of the orthorhombic crystals compared with 3.5 Å of the tetragonal crystals, and because of the higher noncrystallographic symmetry, the diffraction data and improved phases of this space group were primarily used for model building. For brevity, only the data collection and phasing statistics of the orthorhombic crystals are included here and a detailed description of the structure determination procedure will be reported elsewhere. The orthorhombic crystals were grown from solutions of enzyme (12 mg/ml) and polyethylene glycol (PEG) 6000 (40 mg/ml), and 50 mM sodium acetate (pH 5.5). The native data set was collected on a MARRESEARCH imaging plate detector at the European Molecular Biology Laboratory, Heidelberg. The diffraction intensities of the derivatives were measured on a STOE imaging plate diffractometer in our laboratory in Münster. The data sets were scaled and evaluated with programs of the CCP4 program suite [Collaborative Computational Project, Number 4, *Acta Crystallogr. Sect. D* **50**, 760 (1994)]. The difference Patterson function of the first useful derivative, Na_2WO_4, was deconvoluted and the heavy-atom binding sites of the second derivative, PIP, were located by a difference Fourier analysis. The MIR phases were improved and extended to 2.9 Å by solvent flattening and fourfold molecular averaging with the RAVE program [T. A. Jones, in *Molecular Replacement*, E. J. Dodson, Ed. (Science and Engineering Research Council, Daresbury, UK, 1992)]. The program O was used for all model building [T. A. Jones, J.-Y. Zou, S. W. Cowan, *Acta Crystallogr. Sect. A* **47**, 110 (1991)]. The high quality of the improved electron density, in conjunction with the amino acid sequence (*4*), allowed for an unambiguous tracing of the main chain. Structure refinement was performed with XPLOR, using the slow-cooling protocol (3000 K) [A. T. Brünger, XPLOR Version 3.1 Manual (Yale Univ. Press, New Haven, CT, 1993)]. The four monomers within the asymmetric unit have been refined with noncrystallographic symmetry (NCS) restraints. Residues involved in packing interactions were excluded from the NCS restraints. The R factor is currently 19.6% (free R factor = 23.3%) [A. T. Brünger, *Nature* **355**, 472 (1992)]) for 51,523 unique reflections in the 8.0 to 2.9 Å shell ($F/\sigma_F > 2$, 82% complete). There was no interpretable density for the NH_2-terminal residues 1 to 8 in any of the four monomers and they are assumed to be disordered. The root-mean-square (rms) deviations for bond distances and angles were 0.018 Å and 2.7°, respectively. The Luzzati plot suggests a coordinate error of 0.35 Å. Only one residue (His^{323}) is in the disallowed regions of the Ramachandran plot.

23. We thank R. Fröhlich for help with data collection and W. N. Lipscomb and J. C. Sacchettini for reviewing the manuscript. Supported by the Deutsche Forschungsgemeinschaft and by the Fonds der Chemischen Industrie. This study is in partial fulfillment of the requirements of T. K. and N. S. for the degree of Dr rer. nat. at Westfälische Wilhelms–Universität, Münster.

19 December 1994; accepted 15 March 1995

Multiple Origins of Lichen Symbioses in Fungi Suggested by SSU rDNA Phylogeny

Andrea Gargas,* Paula T. DePriest, Martin Grube, Anders Tehler

Phylogenetic hypotheses provide a context for examining the evolution of heterotrophic lifestyles. The lichen lifestyle, which is the symbiotic association of fungi with algae, is found in various representatives of Dicaryomycotina, both Ascomycetes and Basidiomycetes. A highly resolved parsimony analysis of small subunit ribosomal DNA (SSU rDNA) sequences suggests at least five independent origins of the lichen habit in disparate groups of Ascomycetes and Basidiomycetes. Because lichen associations arose from parasitic, mycorrhizal, or free-living saprobic fungi, neither mutualism nor parasitism should be construed as endpoints in symbiont evolution.

Lichens are a classic example of symbiosis ["Zusammenleben ungleichnamiger Organismen" (*1*)], with interactions ranging from mutualistic to parasitic (*2*). Hyphae of the fungal symbiont may lie within a matrix of algal cells, adhere to these cells as appressoria, invaginate these cells as haustoria, or occasionally penetrate cell walls and plasmalemmae (*3*). Long-term survival of the lichen association depends on balanced growth of the symbionts, yet this balance does not preclude killing or saprobic digestion of the algal symbiont (*4*). Lichen-forming fungi represent many diverse lineages of Dicaryomycotina (*5*) that traditionally have been studied under the rubric of lichenology. These lineages are not descended from a single lichen-forming ancestor, yet it is not known how many times, and in which groups, the lichen habit originated. By examining the phylogenetic position of lichen-forming fungi relative to saprobic or pathogenic fungi, we can address a fundamental question of symbiont evolution: whether mutualistic symbioses are derived from more parasitic forms (*6*).

To determine the origins of the lichen habit, we included lichen-forming fungi within a phylogenetic analysis of Amastigomycota, members of Eumycota that lack motile stages. The major lineages of Amastigomycota—Basidiomycetes, Ascomycetes, and the paraphyletic zygomycetous fungi (*7*)—have few comparable morphological characters to serve as the basis for phylogenetic hypotheses. For example, the

A. Gargas and P. T. DePriest, Department of Botany, NHB-166, National Museum of Natural History, Smithsonian Institution, Washington, DC 20560, USA.
M. Grube, Institut für Botanik, Karl-Franzens-Universität Graz, Holteigasse 6, A-8010 Graz, Austria.
A. Tehler, Botaniska Institutionen, Stockholms Universitet, S-106 91, Stockholm, Sweden.

*To whom correspondence should be addressed.